Received April 24, 2020, accepted May 10, 2020, date of publication May 21, 2020, date of current version June 8, 2020.

Digital Object Identifier 10.1109/ACCESS.2020.2996500

Adaptive Electrical Impedance Tomography Resolution Enhancement Using Statistically Quantized Projected Image Sub-Bands

MAJID ZAMANI[1], (Member, IEEE), RICHARD BAYFORD[2], (Senior Member, IEEE), AND ANDREAS DEMOSTHENOUS[1], (Fellow, IEEE)

[1]Department of Electronic and Electrical Engineering, University College London, London WC1E 7JE, U.K.
[2]Department of Natural Sciences, Middlesex University, London NW4 6BT, U.K.

Corresponding author: Andreas Demosthenous (a.demosthenous@ucl.ac.uk)

This work was supported by the Engineering and Physical Sciences Research Council (EPSRC) under Grant EP/T001259/1.

ABSTRACT This paper proposes an adaptive image enhancement method for electrical impedance tomography (EIT). The images are enhanced based on a steerable and multi-scale resolution enhancement algorithm. It is initiated by capturing the spatial variations in decomposition orientations, and decomposition scales of the EIT image. The interpretation of projected image sub-bands is translated into resolution through statistical processes. A steerable filter containing Gaussian basis function derivatives captures the statistical information. Using the regional quantization method (RQM) proposed in this paper, projection weights are computed through spatial statistics of the image sub-bands and tuned adaptively. RQM assigns more resolution to those directional edges which have higher standard deviation and embeds high-order curvatures into the EIT images while suppressing noise. Comparison with conventional image enhancement methods demonstrates the superior performance of RQM. Using RQM it is shown that for 16, 32 and 64 electrode configurations with noise-free recording of 32×32 EIT images the number of electrodes can be reduced by 5, 7 and 12 respectively without loss of detail.

INDEX TERMS Adaptive resolution enhancement, contrast improving index, distortion embedding, electrical impedance tomography, electrodes optimization, local statistics, signal-to-noise ratio, steerable filter.

I. INTRODUCTION

Electrical impedance tomography (EIT) provides a continuous, real-time and non-invasive imaging technique for measuring the internal impedance fluctuations of a body from a series of surface electrodes placed on it [1]. In recent years there has been considerable interest in monitoring regional lung functionality using EIT, especially when designing patient-specific ventilation systems which assist clinicians in the reduction of lung non-functionalities and improved regional air exchange. A number of wearable EIT systems in the form of a belt around the thorax with embedded electronics have been recently developed [2]–[7]. They usually use at least 16 electrodes for adequate image quality.

To achieve acceptable image quality a common design strategy is to increase the number of electrodes which results in a larger EIT system with increased power demands. Resolution enhancement [8]–[12] can be employed to either enhance the image quality or reduce the number of electrodes while maintaining the image quality with a relatively small power increase. In the case of neonates the interest is to reduce the bulk by reducing the number of electrodes since there is very limited space for monitoring lung functionality. In other applications enhancement is necessary when a conventional EIT image has insufficient detail, for example where clinicians are using EIT on adult patients or the application of EIT to reliably extract motor commands to control a hand prosthesis [13].

This paper proposes a new adaptive multi-scale spatial resolution enhancement algorithm exploiting distortion embedding in such a way that low contrast features have more visibility. Its performance is investigated and compared against three conventional image enhancement methods [14]–[16] with two metrics. 1) Pixel detection ratio (PDR); this investigates image pixel recovery in noisy conditions. 2) Contrast improvement index (CII); this compares the

The associate editor coordinating the review of this manuscript and approving it for publication was Wuliang Yin.

proposed resolution enhancement against conventional image enhancement methods using synthetic phantoms. A third metric, $Electrodes_{Opt}$, is used to identify the number of redundant electrodes in EIT systems by considering the signal-to-noise (SNR) of the enhanced and original EIT images.

The rest of the paper is organized as follows. In Section II the image resolution enhancement algorithm is explained. Section III first compares the noise robustness of the proposed regional quantization method (RQM) against conventional methods when performing edge detection. This is followed by two different tests for resolution enhancement investigation, namely the CII of simulated phantoms and identification of the optimized number of electrodes ($Electrodes_{Opt}$). Concluding remarks are provided in Section IV.

II. ADAPTIVE IMAGE RESOLUTION ENHANCEMENT USING MULTI-SCALE DISTORTION EMBEDDING

In this section, a new method is presented for image regional variation enhancement based on embedding multi-scale two-dimensional (2D) resolution enhancement layers ($\mathbf{L_1}$, $\mathbf{L_2}$ . . ., $\mathbf{L_5}$) within different regions of interest as shown in Fig. 1. The aim is to capture and project the regional variations in both scale and orientation, and to superimpose adaptively weighted features with coarse-fine scales into the original image. The enhanced image, $I_{\text{Enhanced}}(x, y)$, is

$$I_{\text{Enhanced}}(x, y) = I_{\text{EIT}}(x, y) + \sum_{k=1}^{n} AGa_k(x, y)\, H_k(x, y) \quad (1)$$

where n is the number of kernels used in the steerable convolution, and $AGa_k(x, y)$ is the signal-adaptive gain for K^{th} image convolution. $H_k(x, y)$ is the gradient image obtained by convolving the image $I_{\text{EIT}}(x, y)$ with K^{th} kernel. This can be done by linear spectral decomposition of the EIT image into scale and orientation sub-bands, i.e. separating the image into a series of disjoint scales in different directions.

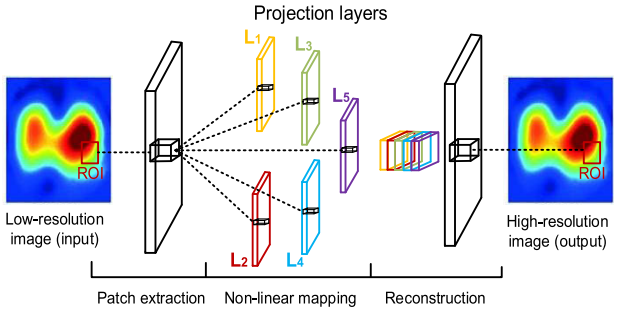

FIGURE 1. Given a low-resolution image, the convolutional layer of the proposed method projects the input image onto different layers. The second layer maps these projections nonlinearly to high-resolution representations. The last layer integrates the resolution enhanced layers ($\mathbf{L_1}$, $\mathbf{L_2}$ . . . , $\mathbf{L_5}$) to produce the final high-resolution image.

Fig. 2 shows the block diagram of the proposed method for image spatial resolution enhancement. The algorithm employs steerable filters [17] using the Gaussian kernel and its derivatives (D_1, D_2, D_3, D_4) to perform the image synthesis. The proposed filter bank forms a very intuitive

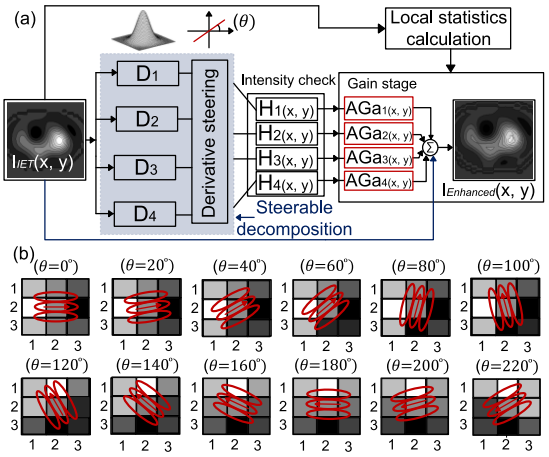

FIGURE 2. Block diagram of the resolution enhancement method. $H_{K\{1,\ldots,4\}}(x, y)$ are the gradients of the steerable convolution with low resolution image $I_{\text{EIT}}(x, y)$. The gradients $H_{K\{1,\ldots,4\}}(x, y)$ are checked for highest intensity and fed to the gain stage. The gain stage $AGa_{K\{1,\ldots,4\}}(x, y)$ adaptively tunes the regional resolution to highlight the hidden variations. (b) Descriptions of the kernel operators used in the steerable convolution stage.

resemblance of EIT images, so they precisely capture the non-stationary localized variations in sub-bands representing different decomposition scales. To realize a steerable convolution, the orientation and scales of the basis kernel functions are swept to better detect geometrical structures in the image. Consider the basic derivatives of Gaussian filter ∂/∂x and ∂/∂y along the x-axis and y-axis respectively:

$$\begin{cases} \dfrac{\partial Gaus(x, y)}{\partial x} = \dfrac{-x}{2\pi\sigma^4}.e^{-\frac{x^2+y^2}{2\sigma^2}} \\ \dfrac{\partial Gaus(x, y)}{\partial y} = \dfrac{-y}{2\pi\sigma^4}.e^{-\frac{x^2+y^2}{2\sigma^2}} \end{cases} \quad (2)$$

where σ is the standard deviation of the Gaussian filter and determines the shape of the filter envelope. Directional Gaussian derivatives $D_{K\{1,\ldots,4\}}(\sigma, \theta)$ at an angle can be generated by a linear combination of a rotation of the basic derivatives of isotropic Gaussian filters:

$$D_{K\{1,\ldots,4\}_{\sigma,\theta}}(x, y) = \cos(\theta).\frac{\partial D_{K\{1,\ldots,4\}}}{\partial x}(x, y) + \sin(\theta).\frac{\partial D_{K\{1,\ldots,4\}}}{\partial y}(x, y). \quad (3)$$

The image derivative $H_{K\{1,\ldots,4\}}(x, y)$ is obtained by convolving $(*)$ the resized image $I_{\text{EIT}}(x, y)$ with the steered Gaussian derivative kernels $D_{K\{1,\ldots,4\}}(\sigma, \theta)$:

$$H_{\sigma,\theta}(x, y) = \left(I_{\text{EIT}}(x, y) * D_{K\{1,\ldots,4\}_{\sigma,\theta}}\right)(x, y). \quad (4)$$

Finally, the magnitude and the direction of image derivatives at a pixel (x, y) are measured as follows:

$$\begin{cases} \|\nabla I(x, y)\| = \left(\left|H_{\sigma,\theta}(x, y)\right|\right)_{\theta\epsilon[0,360]} \\ \theta_m = \left(\left|H_{\sigma,\theta}(x, y)\right|\right)_{\theta\epsilon[0,360]} \end{cases}. \quad (5)$$

Since the regional variations can occur for any magnitude and direction, a set of directional filters whose responses are

selected to cover the whole range of possible orientations is employed. In this work, the steerable filter bank includes derivatives D_1, D_2, D_3, D_4 of the Gaussian kernel function angled in different directions corresponding to eight orientations 0°, 45°, 90°, 135°, 180°, 225°, 270° and 315°.

The set of convolution kernels used in this operation is shown in Fig. 2(b). To distinguish the slight changes in the EIT images, $\sigma = 0.7$ was chosen, with a filter kernel size of 3×3 pixels for the defined rotation angles $\theta \epsilon \{0°, \ldots, 180° + \Delta\theta \ldots 315°\}$ where θ and $\Delta\theta$ are the direction and rotation step size respectively. For each pixel (x, y) the highest filter response is retained for adaptive gain adjustment. RQM realizes pixel-wise adaptive gain tuning to generate the optimal amount of distortion in each projected image after convolution. RQM modifies and generalizes the method described in [18] which adaptively weights the pixels using the local statistics of the original image. In RQM, the gain function is computed for the finalized outputs of the steerable filtering after intensity inspection.

The adaptive gains, $AGa_k(x, y)$, which adaptively weight the projected images at the current pixel (x, y) for the Gaussian derivatives are [18]:

$$AGa_{k=\{1,\ldots,4\}}(x,y) = \begin{cases} -\dfrac{\hat{G}_k^{\max}(x,y)-1}{\sigma I_0^{\max}}\sigma_{I_{\mathrm{EIT}}(x,y)}+\hat{G}_k^{\max}(x,y), & \text{if } U(x,y)=1 \\ 1, & \text{if } U(x,y)=0 \end{cases} \tag{6}$$

where $\sigma_{I_{\mathrm{EIT}}(x,y)}$ is the local standard deviation of the low resolution EIT image with a proper window size centered on the current pixel (x, y), $\sigma I_0^{\max}$ is the maximum value of the local standard deviation in $I_{\mathrm{EIT}}(x, y)$, and $\hat{G}_k^{max}(x, y)$ is the maximum gain in the pixel location (x, y) of the K^{th} image gradient. In (6), the adaptive gain is applied to a specific pixel (x, y) when the non-maximum deletion $U(x, y)$ condition is satisfied; $U(x, y)$ identifies the edge direction [19]. To calculate this parameter the gradient magnitude and direction is defined at each pixel (x, y). The steerable filter calculates the convolution for four different derivatives quantized at eight orientations, and the filter kernel with maximum response is retained:

$$\begin{cases} M(x,y) = \max\limits_{k=\{1\ldots4\}} \left(\left|H_{\sigma,\theta}(x,y)\right|\right) \\ \theta_{\max} = \operatorname{argmax}\limits_{k=\{1\ldots4\}} \left(\left|H_{\sigma,\theta}(x,y)\right|\right) \end{cases}. \tag{7}$$

A 3×1 window is placed along the gradient direction centered on the current pixel (x, y). The binary edge value $U(x, y)$ is defined as follows:

$$U(x,y) = \begin{cases} 1, & \text{if } M(x,y) \text{ is maximum in the} \\ & 3 \times 1 \text{ window along } \theta_{\max}(x,y). \\ 0, & \text{otherwise} \end{cases} \tag{8}$$

When the condition $U(x, y)$ is satisfied, the gain is calculated using the local statistics and the gain factor $\hat{G}_k^{\max}(x, y)$ at the pixel (x, y) of K^{th} gradient image. $\hat{G}_k^{\max}(x, y)$ assigns more visibility to the directional edges with higher standard deviation by superimposing magnified pixels in specific locations of the image as shown in Fig. 3(a). The regional quantization limits are:

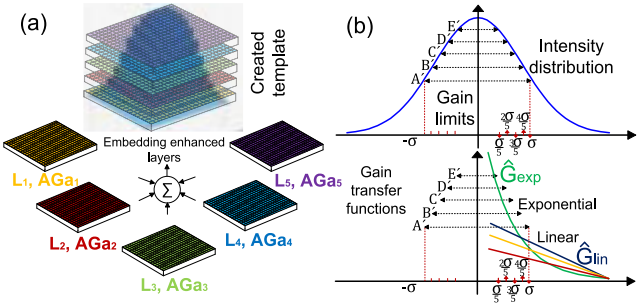

FIGURE 3. **(a) An illustration of multi-scale embedded regional quantization. Each layer (L_1, L_2..., L_5) adaptively modifies image intensity distribution at specific decomposition scale based on a defined gain function (AGa_1, AGa_2 ..., AGa_5). (b) The defined quantization limits for linear or non-linear regional variations mapping.**

$$\hat{G}_{k=\{1,\ldots,k\}}^{\max}(x,y) = \begin{cases} A'\left(\hat{U}+\hat{\omega}\right), \; if \; m_{H_k}+(\frac{4}{5}\sigma_{H_k}) \le H_k < m_{H_k}+\sigma_{H_k} \\ B'\left(\hat{U}+\hat{\omega}\right), \; if \; m_{H_k}+(\frac{3}{5}\sigma_{H_k}) \le H_k < m_{H_k}+(\frac{4}{5}\sigma_{H_k}) \\ \vdots \\ E'\left(\hat{U}+\hat{\omega}\right), \; if \; m_{H_k}+(\frac{1}{5}\sigma_{H_k}) \le H_k < m_{H_k}+(\frac{2}{5}\sigma_{H_k}) \\ \hat{U}, \text{otherwise} \end{cases} \tag{9}$$

where $\hat{U}$ and $\hat{\omega}$ are $\sigma_H^{\max}/\sigma_{H_k}$ and $\sigma_{H_k}/\sigma_{H_1}+\sigma_{H_2}+\ldots+\sigma_{H_4}$, respectively. In the defined limits, m_{H_k} is the overall mean of K^{th} image gradient, σ_{H_k} is the overall standard deviation of K^{th} image gradient and $\sigma_H^{\max}$ is the maximum standard deviation of swept window over K^{th} gradient.

The defined limits in (9) quantize the regional variations using linear or non-linear functions. For example, in the case of non-linear mapping, the gain factors $(A', B', \ldots E')$ can form an exponential function as shown in Fig. 3(b). Finally, a high-resolution image, $I_{\mathrm{Enhanced}}(x, y)$, is reconstructed using the gain-tuned image projections. The weighted convolution layers to the original EIT image are aggregated for generating the high-resolution image.

III. EVALUATION

A. NOISE ROBUSTNESS USING EDGE DETECTION TEST

Edge detection evaluation can be exploited as an objective metric which produces results compatible with standard human-machine perception mechanisms. This suggests that if the image resolution is improved, the percentage of detected edge pixels increases.

Fig. 4 shows the test procedure to compare the performance of the RQM method with three conventional image enhancement methods. Fig. 4(a) shows a noise-free image

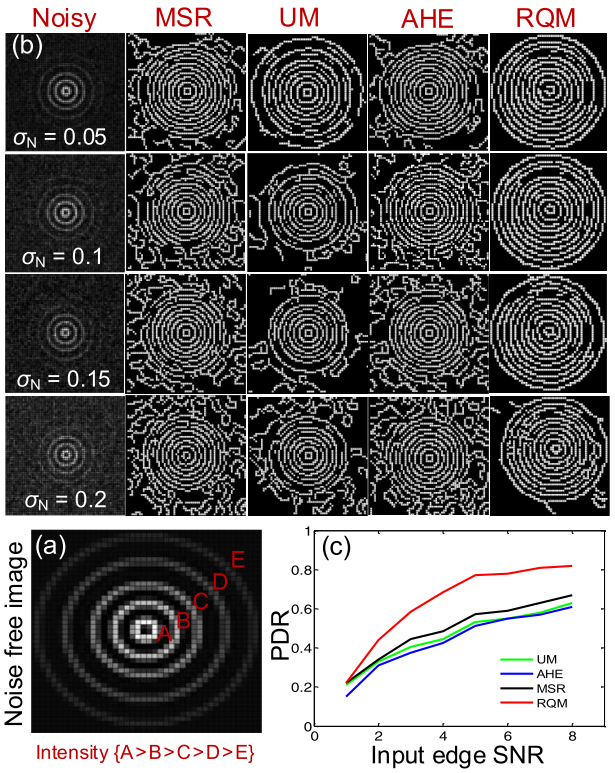

FIGURE 4. (a) Noise free test template. The intensity is changed on each individual circle, from inner to outer layers {A>B>C>D>E}. (b) Gaussian noise is added to the image having standard deviation (σ_N) of 0.05, 0.1, 0.15 and 0.2. Enhanced images using the multi-scale retinex function (MSR), adaptive histogram equalization (AHE), unsharp masking (UM), and regional quantization method (RQM). (c) Percentage of pixel detection ratio (PDR) versus the input edge SNR.

test containing five concentric circles. The intensity of the circles reduces from the first inner circle to the outer circle identified by A, B, C, D and E. In the first column of Fig. 4(b) noise has been generated and superimposed on the noise-free image of Fig. 4(a) using a random Gaussian noise distribution. The noise standard deviation (σ_N) was set to 0.05, 0.01, 0.15 and 0.2. Fig. 4(b) shows from left to right the recovered images with increasing noise levels using four different resolution enhancement methods: multi-scale retinex (MSR) [14], adaptive histogram equalization (AHE) [15], unsharp masking (UM) [16] and RQM. Increasing the noise level adversely affects the structural integrity of the reconstructed images and may result in detecting or introducing wrong edges. As observed in the last column in Fig. 4(b), RQM offers a more solid image recovery even with $\sigma_N = 0.2$.

The pixel detection ratio (PDR) for each resolution enhancement method versus the edge SNR is shown in Fig. 4(c). Identification and summation of the edges in the noise free image of Fig. 4(a) using the Canny edge detector [20] is used as a reference. The number of edge pixels in each circular ring is summed by applying a Canny edge detector to the noise free test template from the inner to the outer perimeters of the rings: $2\pi\left(rin_{(A...E)}\right)+2\pi\left(rout_{(A...E)}\right)$ where *rin* and *rout* are inner and outer radii. For the three alternative methods [14]–[16] and RQM the edges are detected and recorded with the added Gaussian noise ($\sigma_N = 0.05$, 0.1, 0.15 and 0.2). PDR is defined as:

$$\mathrm{PDR} = \frac{\mathrm{TPS}}{\mathrm{TPS} + \mathrm{FP} + \mathrm{MP}} \times 100\% \tag{10}$$

where TPS is the number of truly regained edge pixels, FP (false pixels) are those due to randomly superimposed noise, and MP is the number of missed pixels. This equation is designed to ensure that missed and false pixels carry the same weight in accuracy calculations. Fig. 4(c) shows the superiority of RQM recovery in comparison with the other methods [14]–[16] over a range of edge SNRs.

B. ENHANCEMENT ANALYSIS

Resolution enhancement is measured through contrast evaluation of a chosen region in the original and the enhanced images. The contrast is usually defined as the difference in mean luminance between an object and its surroundings. The statistical assessment uses CII (contrast improvement index) proposed in [21]:

$$\mathrm{CII} = \frac{C_{\mathrm{processed}}}{C_{\mathrm{original}}} \tag{11}$$

where $C_{\mathrm{processed}}$ and C_{original} are the contrasts for a region of interest in the processed and original images, respectively. The contrast C of a region is defined by:

$$C = \frac{f - b}{f + b} \tag{12}$$

where f is the mean gray-level value of the particular region in the image, or *foreground*, and b is the mean gray-level value of the surrounding region or *background*. When an image is composed of textured regions (representative of multiple phantoms) such as EIT images, identifying multiple regions of interest to calculate CII is difficult and time consuming.

A universal operator such as SNR is more suited in the enhancement analysis of EIT images. SNR also is a good metric to quantify the resolution enhancement of RQM, which improves resolution by emphasizing image details and suppressing noise. The SNR of an image is expressed as [22]:

$$\mathrm{SNR} = \frac{\sum_{i=0}^{N-1}\sum_{j=0}^{N-1} U\,(i,j)^2}{\sum_{i=0}^{N-1}\sum_{j=0}^{N-1}\left[U\,(i,j)^2 - \acute{U}\,(i,j)^2\right]} \tag{13}$$

where $U\,(i,j)$ and $\acute{U}\,(i,j)$ represent enhanced and the original images. In the following sections, CII and SNR are used for enhancement improvement analysis of the EIT images from the synthetic phantoms.

C. CII EVALUATION OF SYNTHETIC PHANTOMS

For the evaluation of the local contrast enhancement in the proposed and published methods [14]–[16], images from synthetic phantoms imitating various texture features with amplitude intensity and direction are reconstructed (see Fig. 5). Figs 5(b)-(e) from left to right show the magnified artificial textures from MSR, AHE, UM and RQM respectively.

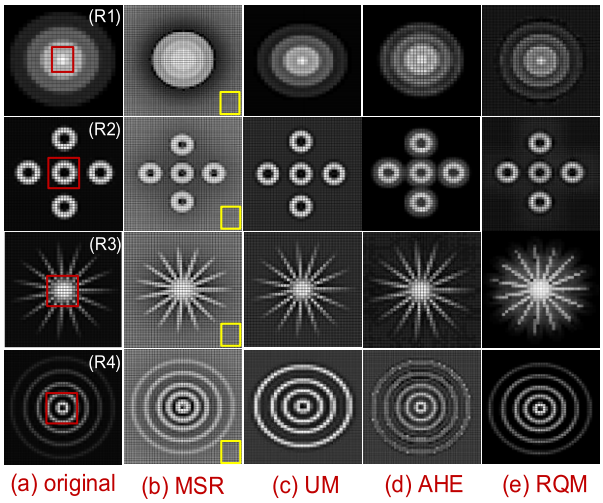

FIGURE 5. The rows (R1 . . . R4) are synthetic simulated images emulating texture features with amplitude intensity and direction variations. Red and yellow squares identify foregrounds and backgrounds. The columns illustrate the images enhanced by four methods: (a) multi-scale retinex (MSR), (b) unsharp masking (UM), (c) adaptive histogram equalization (AHE), and (e) regional quantization method (RQM).

As seen in Fig. 5(e), the embedded regional variations in the image templates (R1-R4) using RQM significantly improve the visual observation. With the aid of the images in Fig. 5, local masks are designed for separating the *foreground* (red squares) from *background* (yellow squares). Table 1 shows the CII comparison results of the different features illustrated in Fig. 5. Note that the multi-scale distortion embedding using RQM performs significantly better than other methods, with adaptive contrast improvement of each specific region.

TABLE 1. CII comparison of generated synthetic phantoms.

Image	CII			
	MSR	UM	AHE	RQM
(R1) Eccentric discs	0.4245	1.034	1.7101	15.237
(R2) Localized circles	0.4009	1.0007	1.4688	14.4665
(R3) Star	0.7524	2.9428	2.8482	10.1094
(R4) Eccentric circles	0.4211	2.2776	3.4546	21.143

D. EIT ELECTRODE OPTIMIZATION ANALYSIS

This section proposes a test to quantify the effect of resolution enhancement on the generated EIT images using different numbers of electrodes, namely, 16, 32 and 64 electrodes.

1) IMAGE RECONSTRUCTION

The EIT phantom image generation uses the boundary data simulator in [23]. The number of recording electrodes, inhomogeneity geometry (shape, size, and position) of phantoms, background conductivity, and inhomogeneity conductivity are all set in the boundary data simulator to emulate various EIT scenarios. The surface potential differences are then reconstructed using GREIT software [24] with 32×32 resolution. Reconstruction of images using fewer than 16 electrodes is not viable as shown in Fig. 6, where regions of errors are highlighted for the 4 and 8 electrode systems.

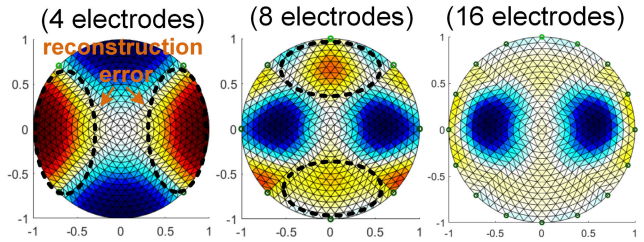

FIGURE 6. The reconstructed EIT images using 4, 8 and 16 electrodes. The reconstruction errors are evident when using 4 and 8 electrodes. The regional error is surrounded by black dotted lines.

2) DATA GENERATION

Two additional components, namely, noise factor and image resizing are embedded into the electrode optimization analysis. Noise has been added to the generated raw EIT voltages (v_r) by superimposing white Gaussian noise ($\sigma_N = 0.025$, 0.05 and 0.075) [25]. The noisy EIT data (v_n) were then reconstructed using GREIT with the recommended setting to ensure optimal performance. Each electrode configuration offers the standard resolution; however, the reconstruction size (32×32) may not be optimal for enhancing image resolution. Resolution enhancement highlights edges, manipulates curvature amplitude and changing slope transitions. Increasing the grid size has key role in changing image resolution spatially but at a computational cost (i.e. number of additions and multiplications).

The EIT images were upscaled using bicubic interpolation with interpolation factors of 2, 4, 8 and 16 before resolution enhancement. The image expansion process aids finding the optimal embedding of the spatial accuracy. For electrode optimization purposes, three EIT image datasets each containing three noise levels and four interpolated images were generated. The three datasets are *E16-IF-noise, E32-IF-noise* and *E64-IF-noise*, where *E16* shows the number of recording electrodes, *noise* denotes the noise level, and *IF* is the interpolation factor.

The procedure used to assess the effect of RQM in optimizing the number of electrodes is shown in Fig. 7(a).

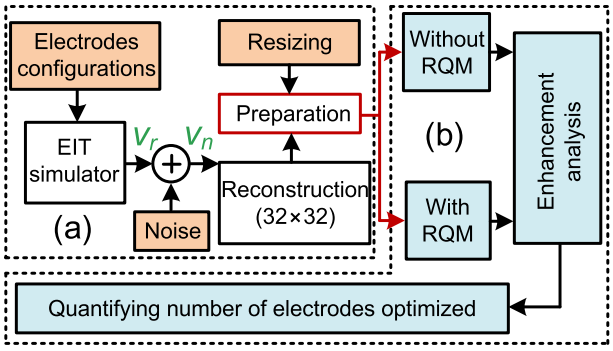

FIGURE 7. Block diagram of the system used to quantify the resolution enhancement and the optimized number of electrodes (a) Data preparation for different numbers of electrodes, noise level and resizing of EIT images. (b) Manipulated (noise enhanced and resized) error-free EIT images are fed to two processing paths, one without RQM and with RQM. The proposed customized setup is used to quantify the resolution enhancement and the number of electrodes optimized.

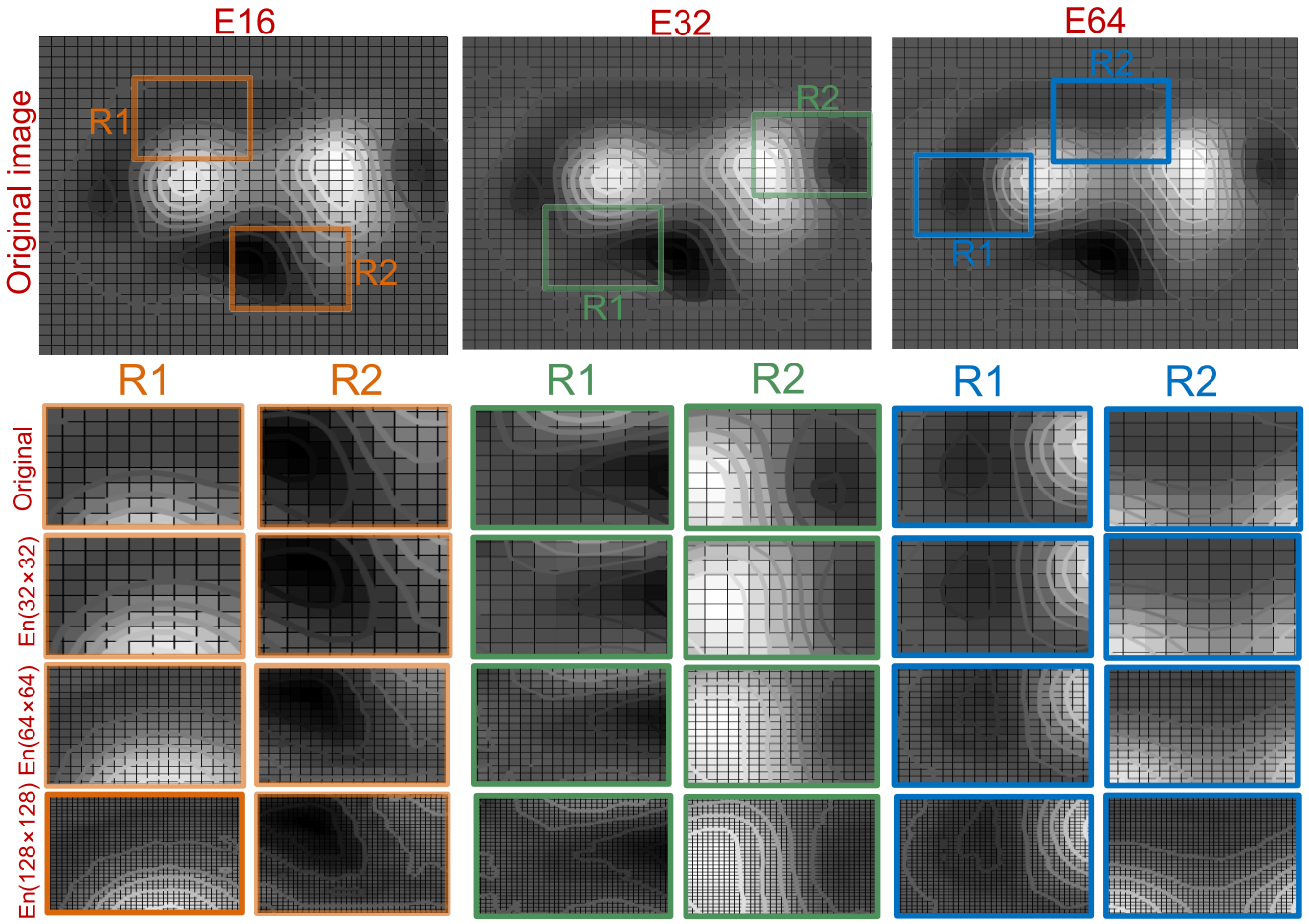

FIGURE 8. The columns are the EIT images from different electrode configurations (*E16, E32,* and *E64*). Color-coded rectangles are superimposed on the EIT images at different regions to visually assess the resolution enhancement. Regions R1 and R2 are placed on the edges and curvatures to capture luminance variation as a result of resolution enhancement. Regions R1 and R2 are different at *E16*, *E32*, and *E64* to include a wide variety of variations in the generated original EIT image. The first row shows the partially sampled original images in regions R1 and R2. The second row shows the resolution enhanced EIT images without resizing En(32 × 32), the third and the fourth rows show the effect of resolution enhancement on the resized EIT images En(64 × 64) and En(128 × 128). Contour plots are superimposed to make the regional variations clearer. Finer resolution is observed as the grid size varies in each column as En(32 × 32) → En(64 × 64) → En(128 × 128) which is the result of embedding high-resolution features in smaller image patches.

In the first path, the reconstructed and manipulated EIT images using different electrode configurations without applying RQM are used for enhancement analysis. The second path applies RQM on EIT images before feeding them to the enhancement analysis unit. The final unit in Fig. 7(b) quantifies the number of electrodes optimized based on the RQM efficacy.

3) SNR ANALSIS OF GENERATED EIT IMAGES AND NUMBER OF ELECTRODES OPTIMIZED

This section studies the effect of RQM on SNR based on the generated EIT image datasets using different numbers of electrodes. To visualize the effectiveness of resolution enhancement using RQM, the original reconstructed images are compared to the enhanced ones after resizing using $IF = 2$ and 4. This is shown in Fig. 8 which also identifies color-coded rectangles at different regions for visual assessment of the resolution enhancement. The regions R1 and R2 are placed on the edges and curvatures of EIT images to capture and visualize enhancement intensity distributions. Columns in Fig. 8 are associated with 16, 32 and 64 electrodes and the rows show the enhanced resolution of 32×32, 64×64 and 128×128 images in R1 and R2. RQM maps hardly distinguishable spatial variations to high-resolution features and higher resolution is embedded with varying the grid size [e.g. $(32 \times 32) \rightarrow (64 \times 64) \rightarrow (128 \times 128)$] as interpreted from Fig. 8. Restoration quality is due to selecting finer image patches and exploring more accurate adaptive gain for reshaping the image variations.

Fig. 9 shows $I_{\text{Enhanced}}(x, y)$ at 128×128 for a different phantom configuration. The enhanced resolution can be observed because the embedded statistical quantized image sub-bands are seen as regional shadowing effects. The phantoms in Fig. 8 and Fig. 9 have non-linearity and show extreme asynchronous filling behaviors in different regions of the left and right lungs. They consist of multiple peaks and valleys, curvatures and edges, suited to validate resolution (contrast) enhancement using RQM.

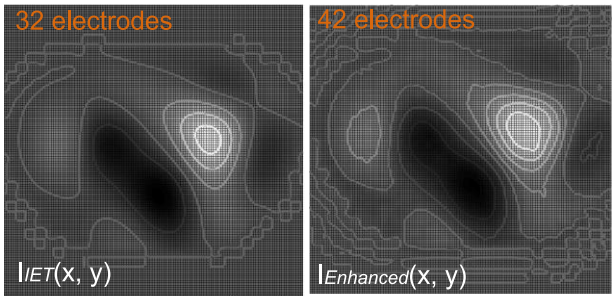

FIGURE 9. Effect of RQM on resolution enhancement. $I_{\text{EIT}}(x, y)$ shows the original EIT image resized to 128 × 128 and $I_{\text{Enhanced}}(x, y)$ shows the enhanced resolution EIT image. The RQM highlights the embedded variations in the EIT images. The difference between the original and the enhanced templates is equivalent to adding 10 more electrodes according to Eq. (14) for *E32*.

In order to quantify the optimized number of electrodes for different conditions, $Electrodes_{Opt}$ is proposed:

$$Electrodes_{Opt} = \frac{\text{SNR}_{\text{Enhanced}}}{\text{SNR}_{\text{Electrode}}} \tag{14}$$

where $\text{SNR}_{\text{Enhanced}}$ is defined based on (13) for enhanced $U(i, j)$ and original $\acute{U}(i, j)$ images. $\text{SNR}_{\text{Electrode}}$ is defined as $\frac{\text{SNR}_{(A-B)}}{(A-B)}$ where A and B represent specific electrode configurations. For example, to quantify the number of electrodes optimized between *E16* and *E32*, the $\text{SNR}_{\text{Electrode}}$ is expressed as $\frac{\text{SNR}_{(32-16)}}{16}$ to identify electrode strength contributing to overall SNR.

Fig. 10 shows the number of electrodes optimized ($Electrodes_{Opt}$) for a specific number of electrodes when the noise level and interpolation factors are considered. The y-axis is the derived $Electrodes_{Opt}$ and the x-axis shows the interpolation factors ($IF = 1$, 2, 4, 8 and 16). $Electrodes_{Opt}$ is also a factor illustrating the number of electrodes resulting in higher resolution in EIT images. For example, in Fig. 10, for *E32* and $IF = 4$, $Electrodes_{Opt} = 10$. This means that with enhancement the standard 32 electrode image can be matched with an enhanced image captured by 22 electrodes or can enhance the 32 electrode image $[I_{\text{Enhanced}}(x, y)]$ to match a standard 42 electrode image. As shown in Fig. 10, at $\{E16, E32 \text{ and } E64\}$, when $IF = 1$ and $\sigma_{\text{N}} = 0$, $Electrodes_{Opt}$ are 5, 7 and 12 respectively. Applying RQM as a back-end processing unit at *E64* results in 12 fewer electrodes needed (and their accompanying components), for the same image quality. According to [6], the overall power consumption of a 12 electrode system is about 4 mW. It could be replaced with a RQM processor consuming much lower power.

Note that the increasing noise level adversely affects the SNR and consequently $Electrodes_{Opt}$. Although the noise level is increased linearly ($\sigma_{\text{N}} = 0.025$, 0.05 and 0.075), the calculated $Electrodes_{Opt}$ shows that RQM performs reverse functioning on the noisy images to retain the SNR values almost unchanged, especially for noise σ_{N} of (0.025 and 0.05).

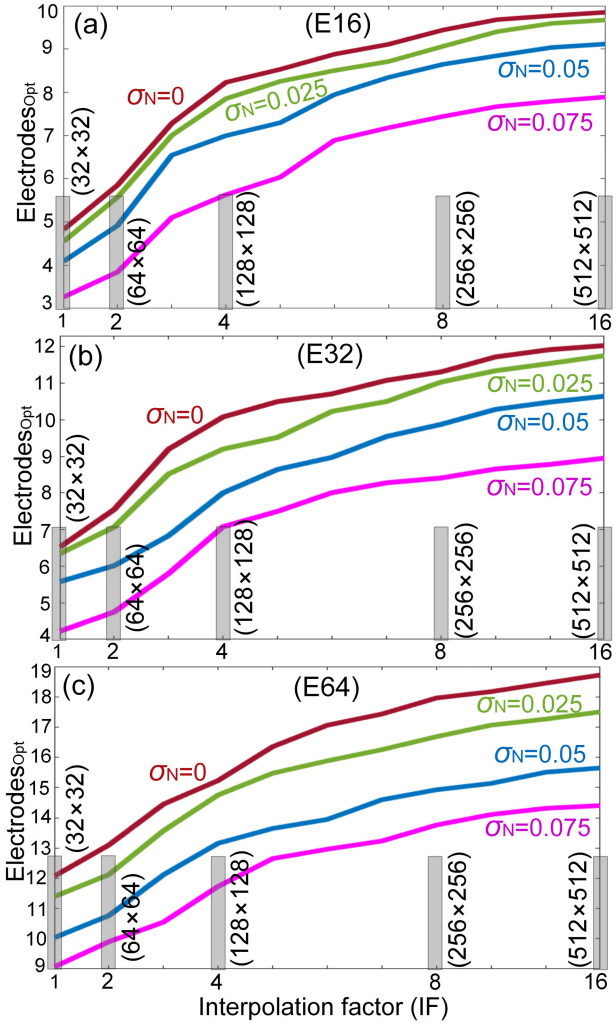

FIGURE 10. Identified number of electrodes optimized ($Electrodes_{Opt}$) versus noise and image grid size. The noise standard deviation was set to $\sigma_{\text{N}} = 0.025$, 0.05 and 0.075 and the grid size was manipulated using bicubic interpolation factors ($1 < IF < 16$). (a), (b) and (c) show the $Electrodes_{Opt}$ graphs for *E16*, *E32* and *E64* respectively. Note that the optimal resolution embedding is a function of image resizing.

Eq. (14) can be alternatively interpreted as the number of recovery electrodes ($Electrodes_{Rec}$) in noisy conditions. For example, at *E32*, RQM consistently assists the recovery of useful information from noisy images, or it can be seen as providing extra electrodes ($Electrodes_{Rec} = 7$ at $IF = 2$ and $\sigma_{\text{N}} = 0.025$). A final point about $Electrodes_{Opt}$ is the effect of *IF*. As shown in Fig. 10, as *IF* increases, the rate of increase of $Electrodes_{Opt}$ is initially high and gradually reduces at higher *IF*. This means that the optimal point for reducing the number of electrodes does not occur when $IF = 1$. This also highlights the fact that resolution embedding is a function of the initial resolution captured by the recording process and the spatial resolution of the image. For example, embedding a high-order curvature in an EIT image depends on the initial resolution and the image grid size. Thus, an optimum *IF* offers a reasonable value of $Electrodes_{Opt}$ at the expense of enhanced image resolution.

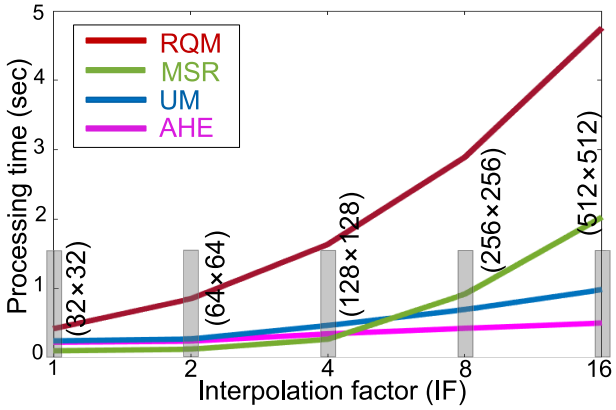

FIGURE 11. Required processing time to generate an enhanced EIT image as a function of image size.

4) COMPUTATIONAL EFFICIENCY

A recognised technique is to compare the computational complexity of algorithms by measuring their execution times, which are effectively correlated with the number of arithmetic operations (i.e. additions or subtractions and multiplications or divisions). For example, in RQM the arithmetic operations are related to extracting rotative sub-bands, calculating adaptive gains and superposition of tuned sub-bands to finally obtain the resolution enhanced EIT image. The processing time required for the proposed and the alternative enhancement algorithms in this paper (MSR, AHE and UM [14]–[16]), were derived and compared when the image size was upscaled using bicubic interpolation. The processing time of each of the algorithms was recorded using the same machine (Intel Dual Core 2.4 GHz processor with 16 GB RAM). As shown in Fig. 11, the RQM processing time increases almost exponentially with respect to the size of the image (or *IF*). It has a longer processing time compared to the other enhancement algorithms,which is as a result of the number of rotational decompositions and identifying image statistics required to spatially enhance the EIT image resolution. When $IF = 4$, the RQM processing time is 3.54, 4.79 and 6.26 times longer than UM, AHE and MSR respectively. Another reason contributing to RQM processing time is the choice of decomposition kernel size. In order to enable very deep decomposition, small kernels are utilized to extract desirable local characteristics corresponding to, e.g., edges and curvatures in the image. The RQM achieves better performance but at the cost of processing time. The RQM processing time could be accelerated, for example by enlarging the rotation angle steps in the steerable filter, with possible slight degradation in performance.

IV. CONCLUSION

The adaptive image enhancement proposed in this paper using RQM is a valuable tool for improving resolution of EIT images. RQM effectively utilizes a reverse approach of EIT recording to evaluate the captured information with deep rotational projection of EIT images in different directions $\theta\epsilon\{0°, \ldots, 180° + \Delta\theta \ldots 315°\}$ and frequency sub-bands ($D_1 \ldots D_4$ in Fig. 2). The deep decomposition approach helps to derive statistical image information in specific directions and sub-bands; therefore, the image data can be adaptively weighted to superimpose high-order transitions and edges resulting in higher resolution in the original images.

Two tests were designed to compare RQM with other image enhancement methods (MSR, AHE and UM). The first test compared the noise robustness of RQM using the pixel detection ratio (PDR). The second test compared the contrast improvement index (CII) of RQM. In both tests the performance of RQM was superior. In a third test the RQM was evaluated based on $Electrodes_{Opt}$ to relate enhanced resolution to an equivalent number of electrodes. For noise-free electrodes at $\{E16, E32$ and $E64\}$, $Electrodes_{Opt}$ showed that the number of electrodes are reduced by 8, 10, and 15 respectively at $IF = 4$. Alternatively, the image enhancement can be interpreted as additional electrodes to transform them into $\{E24, E42$ and $E79\}$. Two additional parameters were also considered in $Electrodes_{Opt}$ analysis including σ_N (0.025, 0.05 and 0.075) and interpolation factor ($1 < IF < 16$). The noise tests showed that RQM assists image recovery and optimal resolution enhancement occurs at higher grid sizes (e.g. 64×64 at $E16$). The results potentially promise high resolution and/or compact EIT systems which can be used in clinical or portable applications.

REFERENCES

[1] B. Brown, "Electrical impedance tomography (EIT): A review," *J. Med. Eng. Technol.*, vol. 27, no. 3, pp. 97–108, Jan. 2003.
[2] Y. Wu, D. Jiang, A. Bardill, R. Bayford, and A. Demosthenous, "A 122 fps, 1 MHz bandwidth multi-frequency wearable EIT belt featuring novel active electrode architecture for neonatal thorax vital sign monitoring," *IEEE Trans. Biomed. Circuits Syst.*, vol. 13, no. 5, pp. 927–937, Oct. 2019.
[3] Y. Wu, D. Jiang, A. Bardill, S. de Gelidi, R. Bayford, and A. Demosthenous, "A high frame rate wearable EIT system using active electrode ASICs for lung respiration and heart rate monitoring," *IEEE Trans. Circuits Syst. I, Reg. Papers*, vol. 65, no. 11, pp. 3810–3820, Nov. 2018.
[4] M. H. Lee, G. Y. Jang, Y. E. Kim, P. J. Yoo, H. Wi, T. I. Oh, and E. J. Woo, "Portable multi-parameter electrical impedance tomography for sleep apnea and hypoventilation monitoring: Feasibility study," *Physiolog. Meas.*, vol. 39, no. 12, Dec. 2018, Art. no. 124004.
[5] Swisstom AG. (2016). *Swisstom BB2 Product Information*. Accessed: Feb. 10, 2019. [Online]. Available: http://www.swisstom.com/en/products/swisstom-bb2_en
[6] S. Hong, J. Lee, J. Bae, and H.-J. Yoo, "A 10.4 mW electrical impedance tomography SoC for portable real-time lung ventilation monitoring system," *IEEE J. Solid-State Circuits*, vol. 50, no. 11, pp. 2501–2512, Nov. 2015.
[7] Y. Jiang and M. Soleimani, "Capacitively coupled resistivity imaging for biomaterial and biomedical applications," *IEEE Access*, vol. 6, pp. 27069–27079, 2018.
[8] J.-L. Starck, F. Murtagh, E. J. Candes, and D. L. Donoho, "Gray and color image contrast enhancement by the curvelet transform," *IEEE Trans. Image Process.*, vol. 12, no. 6, pp. 706–717, Jun. 2003.
[9] H. Demirel and G. Anbarjafari, "IMAGE resolution enhancement by using discrete and stationary wavelet decomposition," *IEEE Trans. Image Process.*, vol. 20, no. 5, pp. 1458–1460, May 2011.
[10] A. M. Mendonca and A. Campilho, "Segmentation of retinal blood vessels by combining the detection of centerlines and morphological reconstruction," *IEEE Trans. Med. Imag.*, vol. 25, no. 9, pp. 1200–1213, Sep. 2006.
[11] J. Kim, J. K. Lee, and K. M. Lee, "Accurate image super-resolution using very deep convolutional networks," in *Proc. IEEE Conf. Comput. Vis. Pattern Recognit. (CVPR)*, Jun. 2016, pp. 1646–1654.

[12] G. Anbarjafari and H. Demirel, "Image super resolution based on interpolation of wavelet domain high frequency subbands and the spatial domain input image," *ETRI J.*, vol. 32, no. 3, pp. 390–394, Jun. 2010.
[13] Y. Wu, D. Jiang, X. Liu, R. Bayford, and A. Demosthenous, "A human–machine interface using electrical impedance tomography for hand prosthesis control," *IEEE Trans. Biomed. Circuits Syst.*, vol. 12, no. 6, pp. 1322–1333, Dec. 2018.
[14] L. Meylan and S. Susstrunk, "High dynamic range image rendering with a retinex-based adaptive filter," *IEEE Trans. Image Process.*, vol. 15, no. 9, pp. 2820–2830, Sep. 2006.
[15] T. K. Agarwal, M. Tiwari, and S. S. Lamba, "Modified histogram based contrast enhancement using homomorphic filtering for medical images," in *Proc. IEEE Int. Advance Comput. Conf. (IACC)*, Feb. 2014, pp. 964–968.
[16] A. Polesel, G. Ramponi, and V. J. Mathews, "Image enhancement via adaptive unsharp masking," *IEEE Trans. Image Process.*, vol. 9, no. 3, pp. 505–510, Mar. 2000.
[17] W. T. Freeman and E. H. Adelson, "The design and use of steerable filters," *IEEE Trans. Pattern Anal. Mach. Intell.*, vol. 13, no. 9, pp. 891–906, Sep. 1991.
[18] J. K. Kim, J. M. Park, K. S. Song, and H. W. Park, "Adaptive mammographic image enhancement using first derivative and local statistics," *IEEE Trans. Med. Imag.*, vol. 16, no. 5, pp. 495–502, Oct. 1997.
[19] V. Lacroix, "A three-module strategy for edge detection," *IEEE Trans. Pattern Anal. Mach. Intell.*, vol. PAMI-10, no. 6, pp. 803–810, Nov. 1988.
[20] W. Rong, Z. Li, W. Zhang, and L. Sun, "An improved canny edge detection algorithm," in *Proc. IEEE Int. Conf. Mechatronics Autom.*, Aug. 2014, pp. 577–582.
[21] W. M. Morrow, R. B. Paranjape, R. M. Rangayyan, and J. E. L. Desautels, "Region based contrast enhancement of mammograms," *IEEE Trans. Med. Imag.*, vol. 11, no. 3, pp. 392–406, 1992.
[22] R. C. Gonzalez and R. E. Woods, *Digital Image Processing*, 3rd ed. Upper Saddle River, NJ, USA: Prentice-Hall, 2006.
[23] T. K. Bera and J. Nagaraju, "A MATLAB-based boundary data simulator for studying the resistivity reconstruction using neighbouring current pattern," *J. Med. Eng.*, vol. 2013, May 2013, Art. no. 193578.
[24] A. Adler, J. H. Arnold, R. Bayford, A. Borsic, B. Brown, P. Dixon, T. J. C. Faes, I. Frerichs, H. Gagnon, Y. Gärber, B. Grychtol, G. Hahn, W. R. B. Lionheart, A. Malik, R. P. Patterson, J. Stocks, A. Tizzard, N. Weiler, and G. K. Wolf, "GREIT: A unified approach to 2D linear EIT reconstruction of lung images," *Physiolog. Meas.*, vol. 30, no. 6, pp. S35–S55, Jun. 2009.
[25] F. Braun, M. Proenca, J. Sola, J.-P. Thiran, and A. Adler, "A versatile noise performance metric for electrical impedance tomography algorithms," *IEEE Trans. Biomed. Eng.*, vol. 64, no. 10, pp. 2321–2330, Oct. 2017.

MAJID ZAMANI (Member, IEEE) was born in Tehran, Iran, in 1984. He received the M.Sc. degree in microelectronics from the Islamic Azad University, Science and Research Branch, Tehran, Iran, in 2011, and the Ph.D. degree from University College London (UCL), London, U.K., in 2017. He is currently a Research Associate with the Analog and Biomedical Electronics Group, UCL. His research interests include design and fabrication of advanced and energy-efficient computational systems utilizing pattern recognition, machine learning, and computer vision algorithms, especially for wearable and implantable biomedical applications. He was a recipient of the Overseas Research Scholarship and a UCL Graduate Research Scholarship to pursue his Ph.D. degree and the Best Researcher M.Sc. Student Award.

RICHARD BAYFORD (Senior Member, IEEE) received the M.Sc. degree in industrial systems from Cranfield University, Cranfield, U.K., and the Ph.D. degree from Middlesex University, London, U.K., in 1994. He was appointed Professor of biophysics and engineering with the Department of Natural Sciences, Middlesex University, in 2005. He is also a Visiting Professor with the Department of Electronic and Electrical Engineering, University College London, London, U.K. He has authored more than 300 articles in journals and international conference proceedings. His expertise is in biomedical image/signal processing, electrical impedance tomography, deep brain stimulation, bio-modeling, tele-medical systems, and VLSI design.

Dr Bayford is a Fellow of the Institute of Physics. He was the Editor-in-Chief of Physiological Measurement, Institute of Physics (IOP), from 2008 to 2013. He is on the editorial board of the *International Journal of Biomedical Imaging*. He has Chaired the journals committee of the Institute of Physics and Engineering in Medicine (IPEM).

ANDREAS DEMOSTHENOUS (Fellow, IEEE) received the B.Eng. degree in electrical and electronic engineering from the University of Leicester, Leicester, U.K., in 1992, the M.Sc. degree in telecommunications technology from Aston University, Birmingham, U.K., in 1994, and the Ph.D. degree in electronic and electrical engineering from University College London (UCL), London, U.K., in 1998. He is currently a Professor with the Department of Electronic and Electrical Engineering, UCL, and leads the Analog and Biomedical Electronics Group. He has made outstanding contributions to improving safety and performance in integrated circuit design for active medical devices, such as spinal cord and brain stimulators. He has numerous collaborations for cross-disciplinary research, within the U.K. and internationally. He has authored over 300 articles in journals and international conference proceedings, several book chapters, and holds several patents. His research interests include analog and mixed-signal integrated circuits for biomedical, sensor, and signal processing applications.

Dr. Demosthenous is a Fellow of the Institution of Engineering and Technology and a Chartered Engineer. He was a co-recipient of a number of Best Paper Awards and has graduated many Ph.D. students. He was an Associate Editor, from 2006 to 2007, and the Deputy Editor- in-Chief, from 2014 to 2015 of the IEEE TRANSACTIONS ON CIRCUITS AND SYSTEMS—II: EXPRESS BRIEFS, and an Associate Editor, from 2008 to 2009, and the Editor-in-Chief, from 2016 to 2019 of the IEEE TRANSACTIONS ON CIRCUITS AND SYSTEMS—I: REGULAR PAPERS. He is an Associate Editor of the IEEE TRANSACTIONS ON BIOMEDICAL CIRCUITS AND SYSTEMS and serves on the International Advisory Board of Physiological Measurement. He has served on the technical committees for a number of international conferences, including the European Solid-State Circuits Conference (ESSCIRC) and the International Symposium on Circuits and Systems (ISCAS).